

Design of Bearingless Permanent Magnet Motors Using No Voltage Combined Windings

Jiahao Chen, Ashad Farhan, Martin Johnson, Eric L Severson*

Department of Electrical and Computer Engineering, University of Wisconsin-Madison, Madison, WI, USA

*E-mail: eric.severson@wisc.edu

Keywords: bearingless motor, high speed motor, combined winding, optimization, self-bearing motor.

Abstract

Bearingless motors have zero mechanical loss and no-contact operation, making them a compelling technology for high speed, high reliability applications, such as industrial compressors. However, currently published demonstrations of bearingless motors have been limited to low power levels (≤ 30 kW). This paper investigates the use of a “no voltage” combined motor winding to overcome performance challenges and enable the development of a medium power, high speed bearingless permanent magnet synchronous motor (BPMSM). An optimization framework is developed and used to explore the design space for several designs with different slot and pole numbers. It is shown that candidate designs achieve $> 95\%$ efficiency while requiring $< 5\%$ of the slot space for suspension current.

1 Introduction

Magnetic bearings possess the features of non-contact operation, long working lifetime, and high precision; however, this comes with the expense of significantly increasing the volume and complexity (cost) of the whole motor system [1, 2]. Bearingless motors present a more integrated solution by using a single machine to create both torque and magnetic bearing forces. Nearly all classical motors can be designed as bearingless motors by modifying the stator winding [3].

Historically, bearingless motor windings have been implemented as two separate windings [3], which compete for slot space. In this approach, upwards of 40% of the slot space is allocated to the suspension winding, which degrades the motor performance. More recently, combined windings have been considered, which use the same coils to produce torque and suspension forces [4–7]. The combined windings enable the bearingless motor drive to dynamically allocate slot space between motor and bearing operation, offering the potential to significantly improve motor performance [8].

The highest power bearingless motor test results published to-date are at approximately 30 kW [9, 10] and have not yet met efficiency requirements of high power industrial motor systems [2]. There have recently been renewed efforts to develop high power, high speed, shafted-type bearingless motors in excess of 30 kW [11–14], where they have the potential to be a highly disruptive technology for industrial compressors (i.e., wastewater aeration, HVAC chillers, gas transportation) [2]. These recent attempts are based around BPMSMs and have considered only a limited number of slot-pole combinations. Design challenges related to force ripple have been addressed by introducing skew and/or careful design of the stator geometry, as opposed to considering the impact of space harmonics and winding factors of slot-pole combinations.

The primary contribution of this paper is to propose and optimize BPMSMs utilizing various fractional-slot and integer-slot windings to meet the high performance requirements of high-power, direct-drive industrial compressors. All windings are implemented as combined dual purpose no voltage (DPNV) windings [4] to utilize the slot space more effectively (improving machine performance) while also minimizing the power electronic requirements [15]. This paper presents the first comparison of optimally designed DPNV windings.

This paper first reviews the winding design procedure for DPNV windings and then develops an optimization framework. These results are then used to explore the design space of BPMSMs featuring several popular slot and pole combinations. The paper determines the various slot-pole combinations’ potential to yield a high performance design based on the optimization results. Two of the most promising designs are then investigated in more detail, including an analysis of the rotor’s structural integrity.

2 DPNV Winding Design Steps

All of the bearingless motors considered in this paper utilize a DPNV winding for the reasons described in Section 1. The design procedure developed in [4] is followed for each specified number of slots and pole pairs (note that all windings considered in this paper have been selected to satisfy the DPNV design criteria determined in [4]). This procedure is now illustrated for one of the slot-pole combinations considered: a double layer, three phase winding with $Q = 12$ slots, $p = 1$ pole-pair motor field, and $p_s = 2$ pole-pair suspension field. The design steps are shown when both the stator slot numbering and rotor rotation are in the counterclockwise direction (which is different from [4]).

The first step of the design procedure is to sketch the star of slots, shown in Fig. 1a, with a slot angle $\alpha_p = p360/Q$ elec. deg. Each phasor corresponds to a coil which is assigned to a phase (U , V , or W) by the phase belts indicated by the symbols $\pm u, \pm v, \pm w$. The coils in the negative phase belts ($-u, -v, -w$) are reversed when connected to form a phase winding. This results in the connection star shown in Fig. 1b. The vector sum of each group is the phase’s back-EMF and can be used to calculate the winding distribution factor.

The second step is to re-draw the connection star at the suspension frequency. This is done by changing the slot phasor angle to $\alpha_{p_s} = p_s 360/Q$ elec. deg, shown in Fig. 1c. One can observe that the vector sum of phasors for each phase is zero, indicating that each phase is unable to produce a p_s pole-pair field. To remedy this, the vectors in the shadowed 180° band (i.e., -7 and -8 for phase U) are reversed (meaning that the corresponding coils are connected in the opposite direction). The reversed coils are assigned to coil groups a and c , with the other coils assigned to groups b and d as described in [4]. These

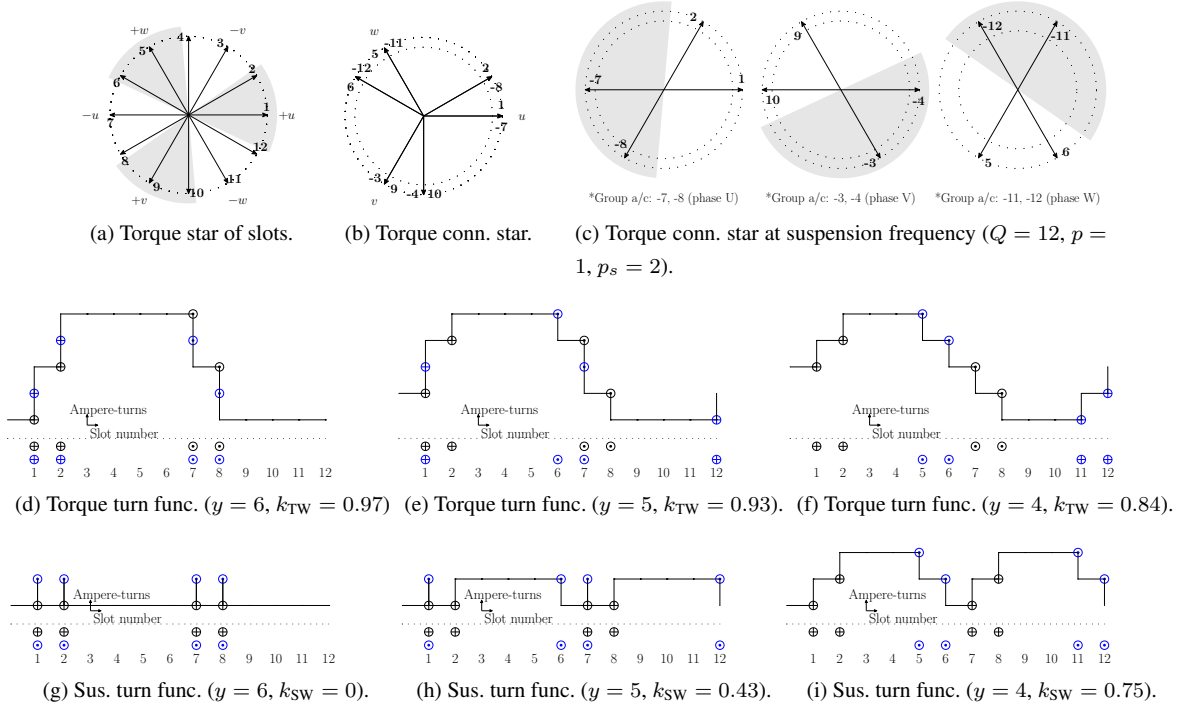


Fig. 1. Winding design steps applied to Q12p1 motor: (a)–(c) coil distribution; (d)–(i) coil pitch.

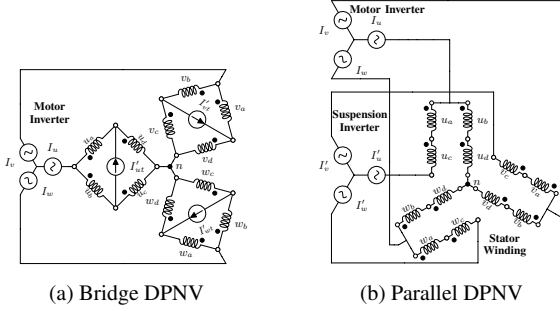


Fig. 2. (a) (b) No voltage combined winding topologies [4].

coil groups are connected to the drive electronics as shown in Fig. 2 (e.g., the inductor u_a indicates coil group a of phase U).

Finally, the coil pitch of the winding is selected. Since the motor and suspension field have a different number of pole-pairs, varying the coil pitch will trade-off how effective the coils are at producing each field. This can be understood through winding factor calculations and with the aid of the mmf waveform or turn function plots in Fig. 1d–1i. When the coil pitch is $y = 6$ or $y = 5$, the suspension turns function has slot-current cancellation, which means that the combined winding is “wasting” current when producing the suspension field. Particularly, in Fig. 1g, all of the current is “wasted,” showing that full pitch coils cannot be used. Reducing the coil pitch y results in a higher amplitude of p_s pole-pair field but a lower amplitude p pole-pair field. Reductions in the torque winding factor can have significant negative implications for the efficiency and torque density of the motor (the authors recommend maintaining a torque winding factor in excess of 0.86). While low suspension winding factor reduces the Newtons per Ampere of the motor, this can be more easily tolerated in a combined winding since current can be re-allocated to suspension purposes when extreme force transients are required.

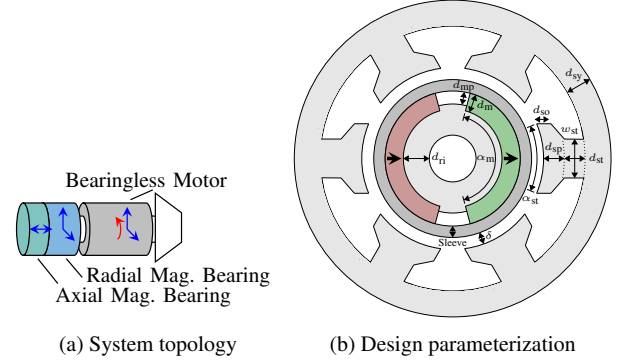


Fig. 3 (a) Proposed system topology for industrial compressors, (b) motor geometry used for optimization.

3 Design and Optimization Framework

The design optimization procedure utilized in this paper is now described. All motors are designed to have a rated power of 50 kW, a rated speed of 30,000 rpm, and the topology of Fig. 3a.

3.1 Windings

Six different no-voltage combined windings listed in Table 1 are considered. The winding designs are uniquely determined by following the procedure of Section 2 with the specified Q stator slots, p torque pole-pairs, p_s suspension pole-pairs, and y coil pitch (in number of slots). The winding factor is also indicated in Table 1 to facilitate a comparison of the windings. Designs where $y = 1$ slot correspond to fractional-slot, concentrated windings. These windings are preferable due to their ease of manufacturing and compact end windings, but add additional harmonic content, possibly resulting in suspension force vector error (control instability) or additional rotor losses.

3.2 Excitation

When evaluating each design, stator slot current is assigned to produce both constant torque and suspension force. This

Algorithm 1 BPMSM Optimization using MOEA/D

Precondition: A design space $\mathcal{B} \subset \mathbb{R}^{11}$. A design template specified by $p, p_s, Q, J_s = 4 \text{ Arms/mm}^2$, packing factor (0.5), and tip speed (150 m/s).

- 1: Initialize population P as $P = \{x_i \mid x_i \in \mathcal{B}, i = 1, 2, \dots, 78\}$.
- 2: **for** $i \leftarrow 1$ to 78 **do**
- 3: $f(x_i) = \text{FITNESS}(x_i)$
- 4: **end for**
- 5: **while** Termination criteria are not met **do**
- 6: **for** $j \leftarrow 1$ to 78 **do**
- 7: Generate j -th trial individual $x_{j,\text{trial}}$ from x_j and another individual in P .
- 8: Evaluate $f(x_{j,\text{trial}}) = \text{FITNESS}(x_{j,\text{trial}})$
- 9: **if** $x_{j,\text{trial}}$ dominates x_j **then**
- 10: $x_j \leftarrow x_{j,\text{trial}}$
- 11: **end if**
- 12: Archive $x_{j,\text{trial}}$.
- 13: **end for**
- 14: **end while**
- 15: Plot Pareto front using the archive (Fig. 4).
- 16: **function** $[O_A, O_B, O_C]^T = \text{FITNESS}(x)$ with $x \in \mathcal{B}$
- 17: Set up FEA simulation with the design template.
- 18: Re-draw motor geometry using x .
- 19: Run transient FEA with two time step sections [17].
- 20: Compute O_A, O_B, O_C in (2).
- 21: **if** Violate constraints in (1) **then**
- 22: $[O_A, O_B, O_C]^T \leftarrow [\infty, \infty, \infty]^T$
- 23: **end if**
- 24: **end function**

is done by exciting the motor and suspension terminals of the winding (see Fig. 2a and 2b) with currents at the synchronous frequency. Currents are assigned so that 5% of the rated coil current is used for suspension fields, with the remaining 95% used to create torque. The stator current density is assumed to be $J_s = 4 \text{ Arms/mm}^2$ with a slot packing factor of 0.5.

3.3 Geometry

The motor geometry considered is shown in Fig. 3b for a $Q = 6, p = 1$ motor. With the minimum air gap length δ fixed to be 0.75 mm, the design consists of eleven free variables (including the sleeve length) as shown in Fig. 3b. Prior to optimization, the procedure documented in [16] is used to create an initial “template” design for each of these dimensions by assuming the permanent magnet tip speed (150 m/s) and the flux density values in the air gap (0.9 T), stator tooth (1.5 T), and stator yoke (1.2 T). This template design is then used to determine the allowable range $\mathcal{B} \subset \mathbb{R}^{11}$ for each of the free variables (taken as 80-120% of the template design values) in an effort to reduce the design space. A carbon fiber sleeve is used to retain the magnets onto the rotor surface. All designs use N40H NdFeB magnets and 29 Gauge M19 steel.

3.4 Optimization

The 11 free variables are optimized using a multi-objective evolutionary algorithm based on decomposition (MOEA/D)

Table 1 Winding Designs Considered.

Name	Q	p	p_s	y	$k_{\text{TD}}(p)$	$k_{\text{TW}}(p)$	$k_{\text{SD}}(p_s)$	$k_{\text{SW}}(p_s)$
Q6p1	6	1	2	2	1.00	0.87	1.00	0.87
Q6p2	6	2	1	1	1.00	0.87	1.00	0.50
Q12p1	12	1	2	5	0.97	0.93	1.00	0.43
Q12p2	12	2	1	3	1.00	1.00	0.71	0.50
Q12p4	12	4	5	1	1.00	0.87	0.71	0.68
Q24p1	24	1	2	9	0.96	0.89	0.84	0.60

* $k_{\text{TD}}, k_{\text{SD}}$: torque and suspension distribution factor, respectively.

* $k_{\text{TW}}, k_{\text{SW}}$: torque and suspension winding factor, respectively.

[18]. The benefits of using MOEA/D over other algorithms are discussed in [19]. Optimization constraints are defined for torque ripple (T_{rip}), force error magnitude (E_m), force error angle (E_a), and force per rotor weight (FRW) as

$$T_{\text{rip}} < 30\%, E_m < 30\%, E_a < 15 \text{ deg}, \text{FRW} > 0.5 \quad (1)$$

The calculation/definition of these performance variables is described in [19]. Consideration of the force vector error is unique to the design of bearingless motors. To ensure stable suspension operation, bearingless motor designers typically target designs with $E_a < 5 \text{ deg}$ [13, 20].

Three objectives, active material cost, efficiency η , and ripple performance sum, i.e.,

$$\begin{aligned} O_A &= -\text{Cost}, O_B = -\eta, \\ O_C &= T_{\text{rip}}/(5\%) + E_m/(5\%) + E_a/(1 \text{ deg}), \end{aligned} \quad (2)$$

are optimized using the concept of Pareto dominance. The detailed optimization process is summarized in Algorithm 1.

3.5 Performance Calculation

The JSOL JMAG transient 2D FEA package is used to evaluate each design candidate generated by the optimization algorithm. Magnet eddy currents cause transient effects at the simulation start, so a “two time-step sections” approach [17] is utilized to allow the eddy currents to quickly reach steady state during the first time-step section (which lasts for 3 electrical period with 24 steps) and then to calculate the performance metrics in the second time-step section (which lasts for a half electrical period with 32 steps). For the Q12p4 design, the second time-step section is prolonged to capture the effect of winding subharmonics. See the discussion in Section 5.1.

The displacement power factor is calculated by extracting the phase angles of the voltage and current fundamental components using the Goertzel algorithm [21] and calculating the cosine of the phase angle difference. This metric is reported in Table 2. The iron loss and the magnet loss are provided by the FEA software while the copper loss is calculated according to [16] considering the winding end length. The windage loss is calculated using an analytic model described in [22].

4 Optimization Results

The design goals are to achieve $> 95\%$ efficiency and torque per rotor volume (TRV) values in the range of 15–50 kNm/m³ in order to be a viable alternative to industrial high speed motors utilizing magnetic bearings [2]. To facilitate the topology comparison, a projection of the 3D Pareto front is shown in Fig. 4 for all six combinations of slots and poles. Since there are three independent objectives, the third objective is indicated by the color of the scatter plot. Only designs with a ripple performance sum O_C less than 20 are shown.

From Fig. 4, the one pole-pair motors (Q6p1, Q12p1, Q24p1) exhibit high efficiency, likely due to the excitation frequency being lowest (i.e., 500 Hz). For the stable operation of a bearingless motor, low ripple performance is preferred (red points in Fig. 4). Therefore, those high ripple Q24p1 and

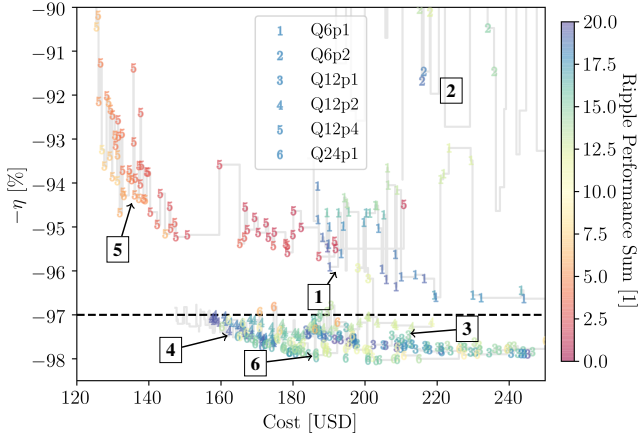


Fig. 4. Pareto fronts of different motor configurations

Table 2 Performance of the Selected Optimal Designs.

Metric	Q6p1	Q6p2	Q12p1	Q12p2	Q12p4	Q24p1
TRV [$\frac{\text{kNm}}{\text{m}^3}$]	32.6	25.0	38.5	40.5	44.5	24.1
FRW [1]	1.21	0.56	0.75	0.85	1.02	0.77
T_{rip} [%]	12.7	6.8	10.1	3.0	1.7	8.3
E_m [%]	21.6	17.1	18.1	18.1	1.7	7.1
E_a [deg]	10.0	10.2	10.0	11.0	1.0	4.1
η [%]	95.01	90.51	97.07	97.28	95.67	96.93
Cost [USD]	194	217	189	184	187	171
Power factor [1]	0.980	0.957	0.972	0.930	0.923	0.958

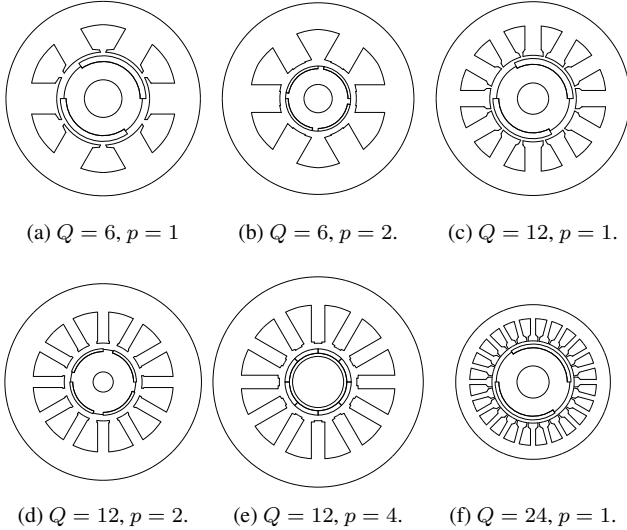


Fig. 5 (a)–(f) Cross-sections of the exemplary optimal designs (drawn at the same scale to facilitate graphical comparison).

Q12p1 designs located at the lower-left corner are not suited to be used as a bearingless motor. On the contrary, the low-cost, low-ripple Q12p4 design and high-efficiency, low-cost, low-ripple Q24p1 design show the most promise to achieve the three objectives and are discussed in more detail in Section 5.

Exemplary designs of each slot pole combination are summarized in Table 2, where bold numbers indicate the best performance metrics. The cross-section of each of these selected designs is shown in Fig. 5. One observes that the Q12p4 design has the thinnest rotor lamination back iron, which improves the rotor dynamics (higher critical speeds). Fig. 5e has a peculiar stator tooth tip shape, which is not seen among non-bearingless motors. Loss component breakdown plots are provided for the exemplary designs in Fig. 6. Designs with high magnet losses (Q6p1 and Q6p2) have the potential for considerable

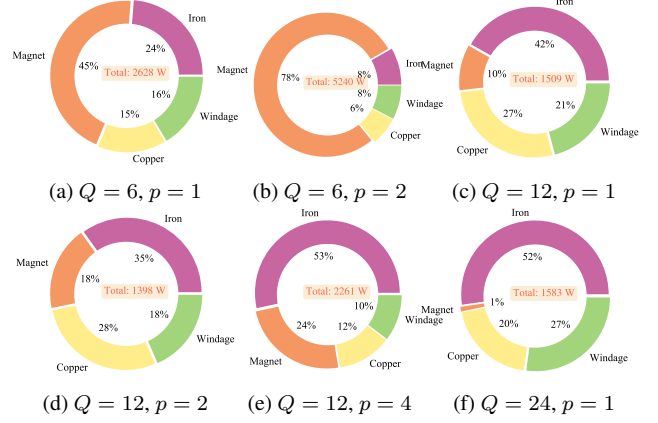


Fig. 6. (a)–(f) loss components of selected optimal designs.

efficiency improvements with magnet segmentation [23, 24], while designs with high iron loss may be improved with the use of ultra thin gauge silicon steels (Q12p2, Q12p4, and Q24p1).

The most intriguing result of the optimization is the strong performance of the Q12p4 design. This design meets the efficiency and TRV design goals while utilizing a double layer fractional slot concentrated winding, which means that coils are wrapped around individual teeth. This makes the winding simple (low cost) to manufacture and significantly reduces the space required for the end winding (improvements in power density over distributed windings). The exemplary design listed in Table 2 has an FRW value of > 1 , which means that the machine can support its rotor weight by using only 5% of the stator slot current. This means that the machine is able to achieve the same motor performance as a “non-bearingless” design. However, the highest number of p value results in the lowest power factor among the six designs, and this is consistent with the analysis in [25].

5 Discussion of Selected Designs

In Section 4, the Q12p4 and Q24p1 design topologies were identified as the most compelling candidate topologies for a high power BPMSM. This section presents an investigation into the model accuracy, design trends, and feasibility of the candidate designs summarized in Table 2 and Fig. 5e and 5f.

5.1 Model Accuracy Implications of Magnet Eddy Currents

Eddy currents are induced in the conductive N40H magnets which can create inaccuracies in the torque and force calculations if not properly modeled. A common modeling mistake is to collect the transient FEA data before the eddy currents have reached steady state. However, it is too computationally expensive to wait for the eddy currents to reach steady state if a single timestep size is used for the entire simulation. The two time-step section approach described in Section 3.5 is depicted in Fig. 7 (the shaded area represents the data used in the performance variable calculation). The Q12p4 design contains sub-harmonics [26] in the suspension turns function, which creates the low frequency (i.e., 500 Hz)* envelope of the force profile shown in the upper-right corner of Fig. 7. This requires that the performance variables be calculated over more

*The synchronous frequency for Q12p4 motor at 30,000 rpm is 2,000 Hz.

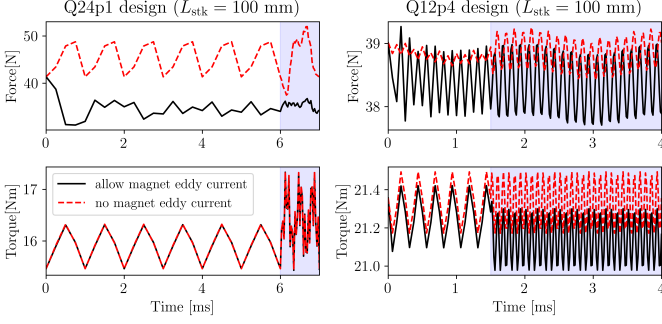


Fig. 7. Impact of magnet eddy currents on FEA results.

electric cycles. While the eddy currents appear to have significant impact on the calculations of both the Q12p4 and Q24p1 designs, both designs are clearly in steady state when the performance variables are calculated, indicating that accurate calculations have been made.

5.2 Tooth Tip Shape

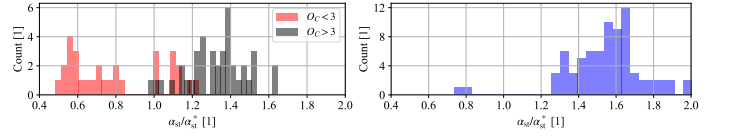
The selected optimal Q12p4 design of Fig. 5e has a peculiar, pinched tooth tip shape (small α_{st}) while the Q24p1 design converged to a conventional, semi-closed tooth tip shape (Fig. 5f). The cause of this difference is now investigated.

First, to determine whether these slot shapes are representative of each topology, the slot shape of all designs on the Pareto front of these topologies (Fig. 4) is investigated, with the results shown in Fig. 8. In this plot, the tooth tip span α_{st} is normalized by the value that corresponds to a straight tooth (denoted as α_{st}^*). Values of $\alpha_{st}/\alpha_{st}^* < 1$ correspond to the pinched shape of Fig. 5e, while $\alpha_{st}/\alpha_{st}^* > 1$ corresponds to the semi-closed shape of Fig. 5f. Clearly the slot shapes depicted in Fig. 5e and 5f are preferred for each of the topologies. We further compared histogram plots (not shown) of the two concentrated winding designs (Q6p2 and Q12p4) to the four distributed winding designs and found that the concentrated windings often converge to pinched or semi-closed tooth shapes while the distributed winding designs mostly converge to semi-closed or straight tooth shapes.

The pinched tooth tip appears to be favored in the concentrated winding designs to minimize leakage flux paths between adjacent stator teeth that are more likely to create disruptive force ripple in concentrated than distributed windings. As shown in Fig. 8a, the Q12p4 design with smaller α_{st} values is more likely to have lower O_C . We found more evidence for this theory through a sensitivity analysis of the selected Q12p4 and Q24p1 designs with respect to variation in α_{st} . Results are shown in Fig. 9a for the Q12p4 design and indicate that small α_{st} values (pinched shape) reduce torque ripple and force vector error but increase the material cost. Interestingly, Fig. 9b shows that for the Q24p1 design, smaller α_{st} values actually increase the ripple performance sum O_C .

5.3 Force Capability

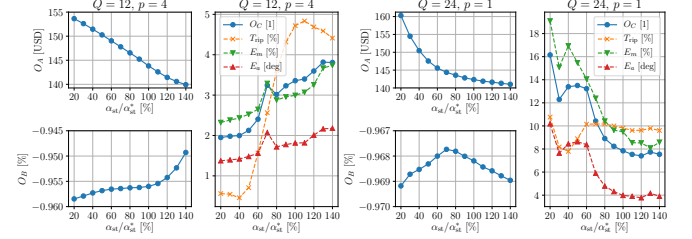
In Fig. 10, the force capability of the two optimal designs as a function of the suspension current under rated current excitation is shown. Compared with the nonlinear force characteristic of the bearingless induction motor [19, Fig. 8], BPMSM has an



(a) Q12p4 (70 individuals)

(b) Q24p1 (75 individuals)

Fig. 8 Histogram plot of α_{st} in the Pareto front designs; α_{st}^* corresponds to the α_{st} when no tooth tip is present.



(a) Q12p4 design (Fig. 5e)

(b) Q24p1 design (Fig. 5f)

Fig. 9. Sensitivity of optimal designs with respect to α_{st} .

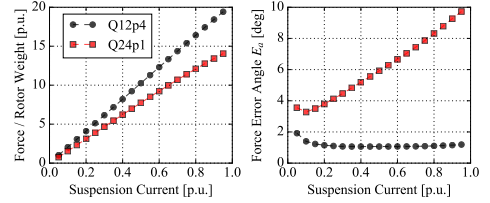


Fig. 10. Force capability of the optimal designs.

almost linear force capability. Both Q12p4 and Q24p1 designs show an impressive capability to create very large forces when all of the stator current is allocated to creating suspension force. Between the Q12p4 and Q24p1, the latter experiences increased force error angle as suspension current increases, while the Q12p4 design maintains a very small error angle under maximum force conditions.

5.4 Structural Integrity

A 2-dimensional analysis was completed to determine if a viable rotor sleeve design is possible for the selected Q12p4 and Q24p1 rotor designs. Carbon fiber was selected as the sleeve material due to its high ultimate strength, low weight, and low-conductivity. A 3.675mm thick sleeve with a 0.675mm under-size were assumed for the Q12p4 design while a 2.5mm thickness, 0.5mm under-sized sleeve was assumed for Q24p1 design. FEA results shows that these sleeves would function at the rated speed with a safety factor over 8 and over 12 for the Q12p4 and Q24p1 designs, respectively.

6 Conclusion

This paper has presented the design optimization of six bearingless permanent magnet motors. Each motor utilizes a popular slot-pole combination where the winding has been designed as a no voltage combined winding. An optimization framework is developed to incorporate both conventional motor design performance metrics (material cost, efficiency, and torque ripple) as well as metrics that are unique to bearingless motors

(force vector error). The optimization results demonstrate that adding the bearingless motor performance metrics modifies the acceptable design space of the different motors. Certain slot-pole combinations (i.e., 12 slot, 8 pole torque, 10 pole sus.) are found to inherently yield substantially better performance than other slot-pole combinations (i.e., 6 slot, 4 pole torque, 2 pole sus.). We theorize that this is due to different harmonic content in the winding turn functions as well as the leakage paths.

The paper concludes by presenting an in-depth analysis of two selected optimal designs, one with a concentrated winding and one with a distributed winding to demonstrating the model accuracy, implications of the stator tooth tip shape, potential to produce high suspension forces without saturation, and structural integrity. The 12-slot concentrated winding design looks particularly promising for a high power, high performance application and will be the subject of a subsequent study.

7 References

- [1] M. Kasarda, "An overview of active magnetic bearing technology and applications," *The shock and vibration digest*, vol. 32, no. 2, pp. 91–99, 2000.
- [2] J. Chen, J. Zhu, and E. L. Severson, "Review of bearingless motor technology for significant power applications," *IEEE Transactions on Industry Applications*, pp. 1–12, 2019.
- [3] A. Chiba, T. Fukao, O. Ichikawa, M. Oshima, M. Takemoto, and D. Dorrell, *Magnetic Bearings and Bearingless Drives*. Newnes, 2005.
- [4] E. L. Severson, R. Nilssen, T. Undeland, and N. Mohan, "Design of dual purpose no-voltage combined windings for bearingless motors," *IEEE Transactions on Industry Applications*, vol. 53, no. 5, pp. 4368–4379, Sept 2017.
- [5] T. Halmeaho, T. Haarnoja, A. Manninen, J. Pippuri, J. Keränen, and K. Tammi, "Magnetic bearing as switched reluctance motor-feasibility study for bearingless switched reluctance motor," in *2013 International Electric Machines & Drives Conference*. IEEE, 2013, pp. 401–408.
- [6] A. Chiba, K. Sotome, Y. Iiyama, and M. Azizur Rahman, "A novel middle-point-current-injection-type bearingless pm synchronous motor for vibration suppression," *Industry Applications, IEEE Transactions on*, vol. 47, no. 4, pp. 1700–1706, 2011.
- [7] H. Mitterhofer, B. Mrak, and W. Gruber, "Comparison of high-speed bearingless drive topologies with combined windings," *Industry Applications, IEEE Trans on*, vol. 51, no. 3, pp. 2116–2122, May 2015.
- [8] K. Raggl, T. Nussbaumer, and J. W. Kolar, "Comparison of separated and combined winding concepts for bearingless centrifugal pumps," *J. Power Electron*, vol. 9, no. 2, pp. 243–258, 2009.
- [9] C. Redemann, P. Meuter, A. Ramella, and T. Gempp, "30kw bearingless canned motor pump on the test bed," in *Seventh International Symp. on Magnetic Bearings, August 23-25, 2000, ETH Zurich*, 2000.
- [10] G. Munteanu, A. Binder, and T. Schneider, "Loss measurement of a 40 kw high-speed bearingless pm synchronous motor," in *Energy Conversion Congress and Exposition (ECCE), 2011 IEEE*. IEEE, 2011, pp. 722–729.
- [11] Y. Fu, M. Takemoto, S. Ogasawara, and K. Orikawa, "Investigation of a high speed and high power density bearingless motor with neodymium bonded magnet," in *Electric Machines and Drives Conference (IEMDC), 2017 IEEE International*. IEEE, 2017, pp. 1–8.
- [12] R. Jastrzebski, P. Jaatinen, H. Sugimoto, O. Pyrhönen, and A. Chiba, "Design of a bearingless 100 kw electric motor for high-speed applications," in *Electrical Machines and Systems (ICEMS), 2015 18th International Conference on*. IEEE, 2015, pp. 2008–2014.
- [13] R. P. Jastrzebski, P. Jaatinen, O. Pyrhönen, and A. Chiba, "Design of 6-slot inset pm bearingless motor for high-speed and higher than 100kw applications," in *Electric Machines and Drives Conference (IEMDC), 2017 IEEE International*. IEEE, 2017, pp. 1–6.
- [14] Y. gu Kang and E. L. Severson, "Optimal design of 50kw concentrated winding bearingless motor," in *2018 IEEE Energy Conversion Congress and Exposition (ECCE)*. IEEE, 2018, pp. 4411–4418.
- [15] E. L. Severson, "Reduced hardware parallel drive for no voltage bearingless motors," in *2018 International Power Electronics Conference (IPEC-Niigata 2018-ECCE ASIA)*. IEEE, 2018, pp. 4020–4027.
- [16] N. Bianchi, S. Bolognani, M. Pre, and G. Grezzani, "Design considerations for fractional-slot winding configurations of synchronous machines," *Industry Applications, IEEE Transactions on*, vol. 42, no. 4, pp. 997–1006, July 2006.
- [17] J. Chen and E. L. Severson, "Design and modeling of the bearingless induction motor," in *2019 IEEE International Electric Machines and Drives Conference (IEMDC), Miami, USA, May 2019*, pp. 1–7.
- [18] Q. Zhang and H. Li, "Moea/d: A multiobjective evolutionary algorithm based on decomposition," *IEEE Transactions on evolutionary computation*, vol. 11, no. 6, pp. 712–731, 2007.
- [19] J. Chen and E. L. Severson, "Optimal design of the bearingless induction motor for industrial applications," in *2019 IEEE Energy Conversion Congress and Exposition (ECCE), September 2019, Baltimore, MD, USA.*, May 2019, pp. 1–7.
- [20] P. Jaatinen, R. P. Jastrzebski, O. Pyrhönen, and A. Chiba, "Improving of bearingless 6-slot ipm motor radial force characteristics using rotor skew," in *2017 IEEE International Electric Machines and Drives Conference (IEMDC)*. IEEE, 2017, pp. 1–7.
- [21] M. Carraro and M. Zigliotto, "Automatic parameter identification of inverter-fed induction motors at standstill," *IEEE Transactions on Industrial Electronics*, vol. 61, no. 9, pp. 4605–4613, Sep. 2014.
- [22] Y. Kang and E. Severson, "Optimization framework for a large high speed bearingless permanent magnet motor," in *Sixteenth International Symposium on Magnetic Bearings*, 2018, pp. 1–10.
- [23] M. Ashabani and Y. A. I. Mohamed, "Multiobjective shape optimization of segmented pole permanent-magnet synchronous machines with improved torque characteristics," *IEEE Transactions on Magnetics*, vol. 47, no. 4, pp. 795–804, April 2011.
- [24] T. Matsuzaki, M. Takemoto, S. Ogasawara, S. Ota, K. Oi, and D. Matsushashi, "Operational characteristics of an ipm-type bearingless motor with 2-pole motor windings and 4-pole suspension windings," *IEEE Transactions on Industry Applications*, vol. 53, no. 6, pp. 5383–5392, Nov 2017.
- [25] Z. Liu and A. Chiba, "Optimum pole number combination for high-speed high-power bpm bearingless motor," in *The 16th International Symposium on Magnetic Bearings (ISMB16)*, 2018.
- [26] J. Pyrhonen, T. Jokinen, and V. Hrabovcova, *Design of rotating electrical machines*. John Wiley & Sons, 2013.